Journal of Crystal Growth 386 (2014) 16–21

Contents lists available at ScienceDirect

Journal of Crystal Growth

journal homepage: www.elsevier.com/locate/jcrysgro

Growth, characterization, and magnetic properties of a Li(Mn,Ni)PO_4 single crystal

Kunpeng Wang [a], Andrey Maljuk [b], Christian G.F. Blum [b], Thomas Kolb [a], Carsten Jähne [a], Christoph Neef [a], Hans-Joachim Grafe [b], Lars Giebeler [b], Hubert Wadepohl [d], Hans-Peter Meyer [c], Sabine Wurmehl [b], Rüdiger Klingeler [a,*]

[a] Kirchhoff Institute for Physics, Heidelberg University, INF 227, D-69120 Heidelberg, Germany
[b] Leibniz Institute for Solid State and Materials Research (IFW) Dresden, D-01171 Dresden, Germany
[c] Institut für Geowissenschaften, Heidelberg University, D-69120 Heidelberg, Germany
[d] Anorganisch-Chemisches Institut, Heidelberg University, D-69120 Heidelberg, Germany

ARTICLE INFO

Article history:
Received 27 March 2013
Received in revised form
20 August 2013
Accepted 25 August 2013
Communicated by V. Fratello
Available online 7 September 2013

Keywords:
Nickel-doped $LiMnPO_4$
Single crystal
Traveling-solvent floating-zone
Lithium-ion batteries
Magnetoelectrics

ABSTRACT

$LiMn_{0.95}Ni_{0.05}PO_4$ single crystals have been grown for the first time by the travelling-solvent floating-zone method at low argon pressure. The grown sample exhibits large single crystalline grains as revealed by means of polarization microscopy, X-ray Laue back scattering, and single-crystal X-ray diffraction. The composition of the crystal was determined by Energy-dispersive X-ray (EDX) spectroscopy. $LiMn_{0.95}Ni_{0.05}PO_4$ orders in an orthorhombic olivine-like structure as expected and phase purity was confirmed by powder X-ray diffraction. An oriented cuboid with size of $2.4 \times 2.5 \times 2.7\ mm^3$ along *a*, *b*, and *c* crystalline directions, respectively, was used for anisotropic magnetic measurements.

1. Introduction

While all end-member olivine phosphates $LiMPO_4$ (M=Mn, Fe, Co, or Ni) exhibit antiferromagnetic spin order and a large magnetoelectric effect in the magnetically ordered phase, the interest in these materials has been further boosted by the recent discovery of unusual ferrotoroidic domains in $LiMPO_4$ with M=Co or Ni [1,2]. In addition, olivine phosphates exhibit exceptionally high applicability for electrochemical energy storage in lithium-ion secondary batteries [3]. With regard to potential application in electrochemical energy storage, mixed transition metal ion compounds Li(M,M′)PO_4 are particularly promising cathode materials since the redox voltage increases from Fe to Mn, Ni, Co [4,5]. Indeed, $LiMnPO_4$ provides a competitive next generation cathode material as carbon-coated nanostructured material exhibits stable reversible capacity up to 145 mA h/g and a rather flat discharge voltage curve at 4.1 V [6–8]. Replacing Mn by Ni not only increases the cell voltage but also enhances the electrochemical performance in general by attenuating the distortion of the lattice while in turn improving the kinetic properties [9]. Therefore, Li(Mn,Ni)PO_4 may provide a next step towards high-energy cathode materials.

For detailed studies of the abovementioned phenomena, i.e. changes of the magnetic anisotropy and magnetoelectric coupling, or the evolution of the ferrotoroidic phase upon replacing of Mn by Ni in $LiMnPO_4$ on the one hand or of the anisotropic electric transport and Li diffusion on the other hand, the growth of large and high-quality single crystals is crucial. However, though the investigation of $LiMPO_4$ single crystals will shed light on the strategy to optimize those functional materials further, only a few studies dealing with single crystals have been done so far and doping series with mixed transition metal ions are completely missing. Most of the studies used polycrystalline powder or LiCl-flux grown crystals of $LiFePO_4$, $LiMnPO_4$ and $LiNiPO_4$, which have been available for a few years already [10–13]. For $LiFePO_4$, Chen et al. successfully applied the travelling-solvent floating-zone (TSFZ) technique with relatively fast growth rates between 2 and 4 mm/h and an Ar flow of 300 ml/min for minimizing the volatilization of Li and to obtain a large stoichiometric crystal [14]. It is noteworthy that the TSFZ- and flux-grown crystals provide qualitatively contradicting information on the nature of the transport properties, i.e. whether electronic/ionic conductivity and

* Corresponding author. Tel.: +49 6221 54 9199; fax: +49 6221 54 9869.
E-mail addresses: kunpeng.wang@kip.uni-heidelberg.de (K. Wang), klingeler@kip.uni-heidelberg.de (R. Klingeler).

0022-0248/$ - see front matter © 2013 Elsevier B.V. All rights reserved.
http://dx.doi.org/10.1016/j.jcrysgro.2013.08.032

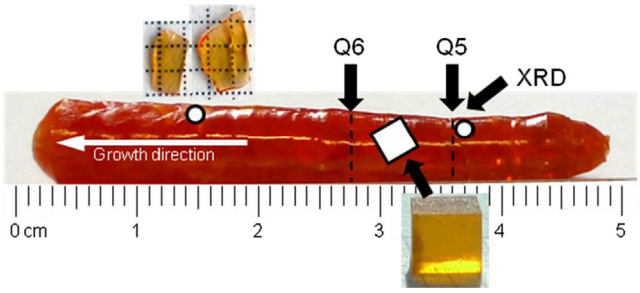

Fig. 1. The as-grown $LiMn_{0.95}Ni_{0.05}PO_4$ single crystal. Q5 and Q6 mark cuts mentioned in the text, the circle indicates the position where the material for the powder XRD has been taken, and two small thin crystal pieces were used for additional optical imaging (see the text). The oriented cuboid was extracted as sketched.

Li-diffusivity are essentially either one- or two-dimensional [10,12]. In addition, the effect of doping on the ionic conductivity has been studied on TSFZ-grown Al-doped and Si-doped single crystals [15,16]. $LiCoPO_4$ single crystals have been grown at Ar pressure of 7 bar [17] while $LiMnPO_4$ TSFZ-grown single crystals were produced at 40 bar Ar pressure or higher [18,19]. Here, we report for the first time on the growth of single crystalline $LiMn_{1-x}Ni_xPO_4$ with $x=0.05$ at low Ar pressure and its initial characterization. The Ni-doped crystals will allow investigation of the changes of magnetic anisotropy and magnetoelectric coupling, which strongly differ in $LiMnPO_4$ and $LiNiPO_4$. The rod size is 50 mm in length with a diameter of 6.0–7.8 mm. Two cube-like single crystals of 10–15 mm^3 volume have been extracted from the rod for further studies (see Fig. 1). Phase purity and crystallinity is confirmed by powder X-ray diffraction as well as by polarized light imaging. Excellent crystal quality is confirmed by a highly anisotropic antiferromagnetic phase transition at $T_N=32.5$ K and a very sharp spin–flop-like magnetic field-driven reorientation in the magnetically ordered phase. While the small level of Ni-doping already yields a significant reduction of the spin–flop field B_{SF} as compared to $LiMnPO_4$, the easy magnetic axis is still parallel to the crystallographic *a* direction. The material at hand therefore provides a first step to the spin reorientation towards the magnetically easy *c*-axis and the formation of the ferrotoroidic phase at high Ni-doping levels.

2. Experimental section

2.1. Crystal growth

Polycrystalline $LiMn_{0.95}Ni_{0.05}PO_4$ was prepared by a solid-state reaction using a stoichiometric mixture of Li_2CO_3 (Chempur 99+%), $MnCO_3$ (Aldrich 99.9+%), NiO (Aldrich 99.9+%) and $NH_4H_2PO_4$ (Chempur 99+%) under flowing argon. The chemical reaction can be expressed as:

$$Li_2CO_3 + 1.9MnCO_3 + 0.1NiO + 2NH_4H_2PO_4 \rightarrow 2LiMn_{0.95}Ni_{0.05}PO_4 + 2.9CO_2\uparrow + 3H_2O\uparrow + 2NH_3\uparrow$$

The mixture of the precursor materials was ground carefully to ensure homogeneity, and then the powder was sintered for 20 h at 800 °C. Subsequently, the product was ground and pressed at 2 kbar (CIP, Engineered Pressure Systems; 2000 bar) and sintered again at 800 °C for 10 h. The $LiMn_{0.95}Ni_{0.05}PO_4$ crystal was grown in a floating zone facility with IR optical heating (Crystal Systems Corporation, Japan). Four 300 W air-cooled halogen lamps were employed. A quartz tube with 2 mm wall thickness was used as the growth chamber. The applied Ar pressure in the growth chamber was 2 bar. The feed rod was rotated clockwise at a rate of 15 rpm, and the seed anticlockwise 15 rpm. The growth rate was 2.5 mm/h.

2.2. Crystal characterization

The elemental concentration of $LiMn_{0.95}Ni_{0.05}PO_4$ was analyzed on a scanning electron microscope (SEM) LEO 440 with Oxford Inca X-Max 80 detector. The accelerating voltage was 20 kV, working distance ~25 mm, and counting time 100 s (lifetime) at about 10,000 cps.

Powder X-ray diffraction data were collected at room temperature on a STOE Stadi P diffractometer equipped with a 6°-linear position sensitive detector and a curved Ge(111)-monochromator of the Johann-type. Samples were measured with Cu $K_{\alpha 1}$-radiation in the range of $5^\circ \le 2\theta \le 90^\circ$ in transmission geometry (flat sample) with a step size of $\Delta 2\theta = 0.01^\circ$. The powder sample was prepared as a thin layer on a polyacetate film with a collodium/amyl acetate glue. For the Rietveld refinement the software package WinPlotR including Fullprof was used [20]. As structure model, the structure data of undoped $LiMnPO_4$, space group *Pnma* [21], was implemented into the Fullprof program routine according to the standardized data set as provided by the Inorganic Crystal Structure Database (ICSD) [22]. The microstructure and crystal perfection of several samples were investigated by optical microscopy in a polarization microscope Axiovert 25 equipped with a digital camera (both Carl Zeiss). The orientation of the single crystal was determined by the X-ray Laue back-scattering method, which was performed at a Seifert X-ray diffraction system with Mo K_α radiation. The power is 50 kW with a current of 40 mA. The exposure time on the film was 30 min.

Single crystal X-ray measurements were performed at $T=110$ K by means of an Agilent Technologies Supernova-E CCD diffractometer (Mo-K_α radiation, $\lambda=0.7107$ Å, microfocus tube, multilayer mirror optics). A complete shell of data was collected up to $\theta=32^\circ$ from a sample of irregular shape (approx. $0.8 \times 0.5 \times 0.2$ mm^3). Data were corrected for air and detector absorption, Lorentz and polarization effects [23]. A correction for partial illumination of the crystal by the primary X-ray beam was performed along with a numerical absorption correction (Gaussian grid) [20]. Scaling and residual absorption correction were carried out with a semiempirical multiscan method [24]. The structure was solved by the charge flip procedure [25,26] and refined by full-matrix least squares methods based on F^2 against all unique reflections [27]. All hydrogen atoms were given anisotropic displacement parameters. Refinement of the populations of Mn and Ni on the same site (point symmetry *m*) with the sum of their site occupation factors (sof) fixed to 0.5 and the anisotropic displacement parameters constrained to be equal did not converge. However, when the sof of Ni was held fixed at 0.025, the sof of Mn refined to 0.468 (1), corresponding to a Mn:Ni atomic ratio 0.94:0.05, close to the expected (0.95:0.05). Further details of the crystal structure investigation may be obtained from FIZ Karlsruhe [28] on quoting the deposition number CSD-426432.

The temperature dependence of the static magnetic susceptibility $\chi=M/B$ was measured both after cooling in zero magnetic field (ZFC) and in the actual probing field (FC), respectively. The data were collected at temperature from 2 to 380 K in an applied external magnetic field of $B=0.1$ T applied along the three crystalline axes of an oriented cuboid by means of a Quantum Design MPMS XL5 SQUID magnetometer. The field dependence of the magnetization was studied at $T=1.8$ K in magnetic fields up to 5 T.

3. Results and discussion

Fig. 1 shows the as-grown rod of $LiMn_{0.95}Ni_{0.05}PO_4$ with a 6–7.8 mm diameter and 50 mm length. From Fig. 1 we can see that the material displays orange transparent color, which is the same as in undoped $LiMnPO_4$ [16]. The phase purity of the grown crystal

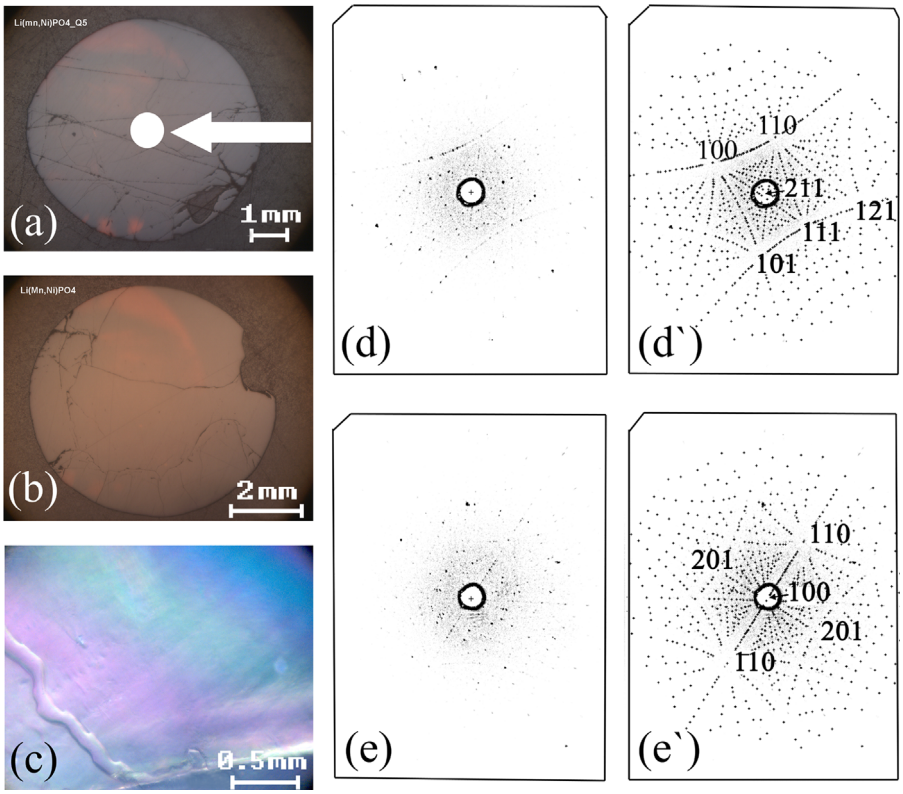

Fig. 2. Optical images in polarized light of both the (a) Q5, and (b) Q6 cross sections cut from the initial part of the $LiMn_{0.95}Ni_{0.05}PO_4$ crystal, as well as the polarization image of (c) a 2 mm thick plate; X-ray Laue back scattering images of the (d) experimental, and (d′) simulated patterns with orientation, as well as the (e) experimental, and (e′) simulated patterns with axis. The Laue pattern was determined at the position labeled by the white circle in part (a) of this figure.

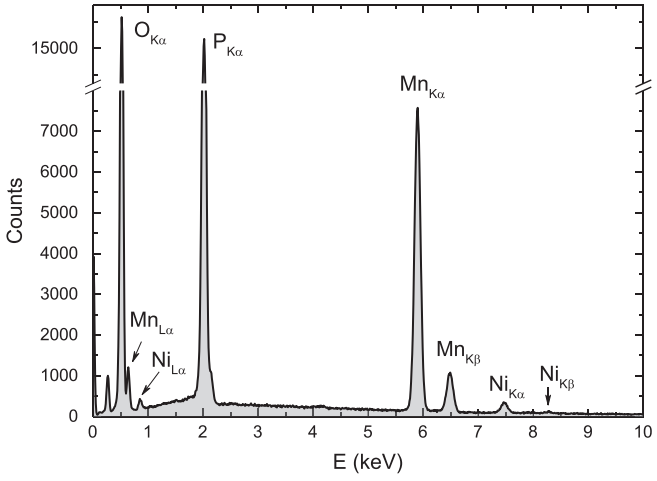

Fig. 3. Energy dispersive X-ray spectrum of the $LiMn_{0.95}Ni_{0.05}PO_4$ crystal.

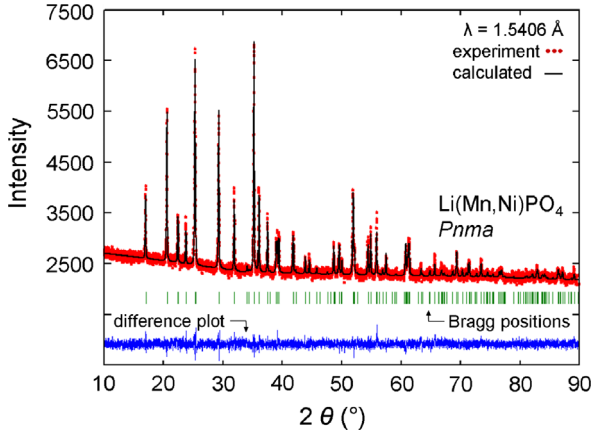

Fig. 4. X-ray powder diffraction pattern and refinement (R_p=1.70, R_{wp}=2.17, R_e=2.03, χ^2=1.14) of a powdered $LiMn_{0.95}Ni_{0.05}PO_4$ single crystal.

was checked by powder X-ray diffraction (XRD) on a powdered piece of the single crystal (see Fig. 1). The resulting XRD pattern is shown in Fig. 4. All Bragg reflections are indexed by the structure of $LiMnPO_4$, space group *Pnma* [18]. Additional phases are excluded due to the absence of any additional reflection within the detection limit of the XRD method. The lattice parameters are determined to be a=10.4247(13) Å, b=6.0906(8) Å, and c=4.7358 (6) Å. The unit cell volume of 300.69(11) Å^3 at room temperature is slightly lower than 301.12(3) Å^3 of polycrystalline $LiMnPO_4$ [18]. The reduced unit cell volume of the reported phase may result from replacement of some of the Mn^{2+} by Ni^{2+}. When associating the Ni-doping with negative chemical pressure [29], our results imply $\Delta V/V \approx -1\times10^{-3}$/% Ni. There is no clear hint on a substitution of larger amounts of Mn by Ni owing to the small total amount of nickel. Considering, in addition, that pure $LiNiPO_4$ (V=274.49(1) Å^3) [18] and pure $LiMnPO_4$ form isostructural compounds, no large influence of Ni on the structure of $Li(Mn,Ni)PO_4$ solid solutions is expected. Some Bragg reflections are underestimated by the refined structure model, which corresponds the remaining single crystal contributions to the powder pattern. These contributions can result from preferred orientations and the shape of the grains due to the crystal growth process.

For the cross-sectional polarized light images, an 8 mm thick sample was cross cut from the initial part of the $LiMn_{0.95}Ni_{0.05}PO_4$ crystal rod. The surface of the cylindrical sample toward to the initial part was labeled as Q5, and the other side of the sample was

labeled as Q6. The optical images of the Q5 and Q6 samples in polarized light are shown in Fig. 2(a) and (b), respectively. The transmittance of the polarized light is in most parts homogeneous indicating that the as-grown crystal boule consists of mainly one large grain throughout the entire cross-section. The few areas with high transmission on both surfaces were induced by local stress, which presumably can be eliminated by thermal annealing. Besides the local stress, we also observe a few mechanical scratches and grain boundaries. No significant difference can be observed on both sides of the sample (Q5 and Q6), indicating that the growth conditions of the crystal such as the applied power, growth rate and speed of rotation are relatively stable. The as-grown crystal quality is apparently good as the common macro-defects such as cracks, precipitations, inclusions, striations and bubbles were not observed. To further investigate the defects in the grown crystal, we cut the samples into slices with thickness less than 2 mm (cf. Fig. 1). The polarized microscopic image is shown in Fig. 2(c). Regular interference fringe can be observed, implying that the optical homogeneity of the crystal is good.

The X-ray Laue back-scattering image, which was obtained in the position represented by the white circle in Fig. 2a, of the 8 mm thick cylindrical sample shown in Fig. 2d, is discussed exemplarily below. Similar Laue experiments were done at different spots of all surfaces of the cuboid used for the magnetization experiments (see Fig. 5), giving the same results, which further confirms large single crystalline grains. The Laue data obtained at the white spot region imply that the growth direction does not coincide with one of the main crystal axes. The Laue spots can be clearly observed. Seven diffraction peaks with the highest intensities were selected to simulate the geometric distribution of the Laue spots based on the orthorhombic lattice unit of $LiMnPO_4$. The simulated Laue pattern shown in Fig. 2d′ agrees well with the experimental one, confirming the orthorhombic symmetry. All the diffraction spots were then indexed successfully confirming that the structure of the sample is basically the same as in undoped $LiMnPO_4$. The Laue spot located in the center of the film is indexed as $(2\ 1\ \bar{1})$, which corresponds to the lattice plane parallel to the film. As the sample was cross cut from the $LiMn_{0.95}Ni_{0.05}PO_4$ crystal rod, we can deduce that the crystal was grown along the $\langle 2\ 1\ \bar{1}\rangle$ crystalline direction. The Laue patterns were used to cut the sample along the main crystal directions, as exemplified in Fig. 2e and 2e′ showing

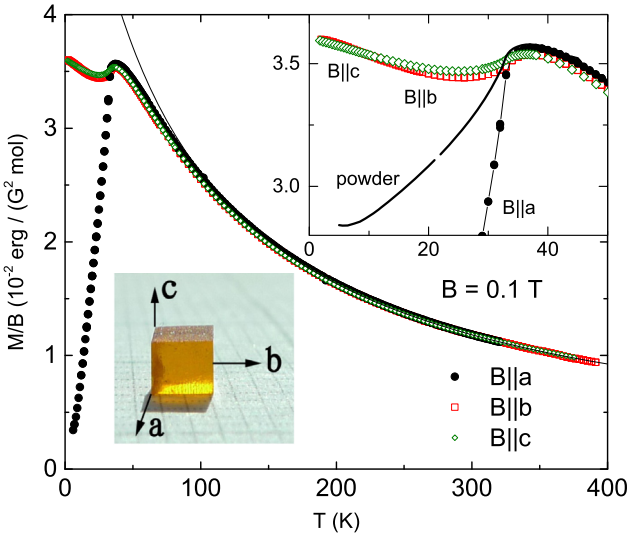

Fig. 5. Static magnetic susceptibility $\chi = M/B$ obtained on the cuboid shown for external magnetic field oriented along the three main crystal axes. The line represents a Curie–Weiss approximation to the average susceptibility $(\chi_a+\chi_b+\chi_c)/3$, the inset highlights the low temperature region and displays the susceptibility obtained on a powder sample.

orientation perpendicular to the (100) plane. The refinement of the single crystal X-ray diffraction data at $T = 110$ K yields the olivine structure known in undoped $LiMnPO_4$. Results, atomic coordinates and equivalent displacement parameters are listed in Tables 1 and 2. The analysis implies a fixed atomic ratio Mn:Ni = 0.95:0.05 on the same position. The unit cell volume of 299.35 A^3 is slightly lower than that deduced from powder XRD data at 300 K (300.69 A^3, see above) which corresponds to a mean volumetric thermal expansion coefficient factor of $\sim 2–3 \times 10^{-5}\ K^{-1}$.

Chemical analysis was performed by means of energy-dispersive X-ray analysis. In order to minimize the measurement uncertainty, three different areas ($50 \times 50\ \mu m^2$) have been measured for deriving the chemical composition (Fig. 3). For the calibration pure $LiMnPO_4$ was used as internal standard. The Li content generally cannot be analyzed by a standard EDX measurement. Oxygen was not determined from the spectra but assumed to be stoichiometric with the cations, Mn^{2+}, Ni^{2+}, and P^{5+}. Accordingly, when normalizing to 100%, Li_2O was neglected. The calculation of the stoichiometric formula is based on 3.5 oxygen atoms per formula unit. The typical EDX spectra exhibit Mn, Ni, P, and O peaks, in addition to the C peak stemming from the coating layer. The results of the analysis are shown in Table 3. For Mn, Ni, and P the atomic ratios nearly match the nominal stoichiometry, i.e. 0.952Mn, 0.058Ni, and 0.996P. The statistical uncertainty as determined by the root mean square deviations from the average values is negligible, i.e. ± 0.001 for Mn, Ni, and P. The average Mn:Ni ratio amount to 94.23:5.77 which is in a good agreement with the initial weight ratio and there are only small deviations at the different spots. This indicates that all the initially used Ni was incorporated in the main phase of $Li(Mn,Ni)PO_4$ and has a rather homogenous Ni distribution.

Table 1
Details on structure refinement and lattice parameters obtained at $T = 110$ K.

Crystal system	Orthorhombic
Space group	*P nma*
θ Range for data collection	3.9–32.3°
Reflections collected	8987
Independent reflections [R_{int}]	564 [0.0395]
Observed reflections [$I > 2\sigma(I)$]	560
Unit cell dimensions	$a = 10.41218(16)$ Å $b = 6.08398(10)$ Å $c = 4.72553(7)$ Å
Volume	299.350(8) Å^3
Index ranges *h*, *k*, *l*	−15 … 15, −9 … 9, −7 … 7
Completeness to $\theta = 25.2°$	99.7%
Absorption correction	Numerical and semi-empirical
Absorption coefficient	4.864 mm^{-1}
Transmission factors: max, min	1.147, 0.114
Extinction coefficient	0.246(9)
Data/restraints/parameters	564/0/42
Goodness-of-fit on F^2	1.152
Final *R* indices [$F_o > 4\,s(F_o)$] $R(F)$, $wR(F^2)$	0.0176, 0.0482
Final *R* indices (all data) $R(F)$, $wR(F^2)$	0.0178, 0.0484
Difference density: rms, max, min	0.099, 0.469, −0.713 e Å^{-3}

Table 2
Atomic coordinates and isotropic atomic displacement parameters U_{eq}.

	x	*y*	*z*	U_{eq}
Mn/Ni	0.2808(1)	0.2500	0.4718(1)	0.009(1)
P	0.4081(1)	−0.2500	0.4094(1)	0.009(1)
O(1)	0.5452(1)	−0.2500	0.2881(3)	0.011(1)
O(2)	0.3387(1)	−0.0488(2)	0.2767(2)	0.011(1)
O(3)	0.4039(1)	−0.2500	0.7313(3)	0.011(1)
Li+	0.5000	−0.5000	0	0.006(1)

Table 3
The chemical composition as determined by EDX analysis on three areas at the (001) surface of the $LiMn_{0.95}Ni_{0.05}PO_4$ crystal. The table shows the experimental data with respect to a pure $LiMnPO_4$ standard in wt%, the average Ø, the root mean square RMS, and the calculated numbers of Mn, Ni, and P cations based on 3.5 oxygens per formula unit (see the text).

	Wt%					Number of cations	
	Area 1	Area 2	Area 3	Ø	RMS		Ø
MnO	47.46	47.29	47.36	47.37	0.07	Mn	0.952
NiO	3.13	3.03	3.01	3.06	0.05	Ni	0.058
P_2O_5	49.41	49.69	49.64	49.58	0.12	P	0.996
Sum	100.00	100.01	100.01	100.01		Sum	2.006

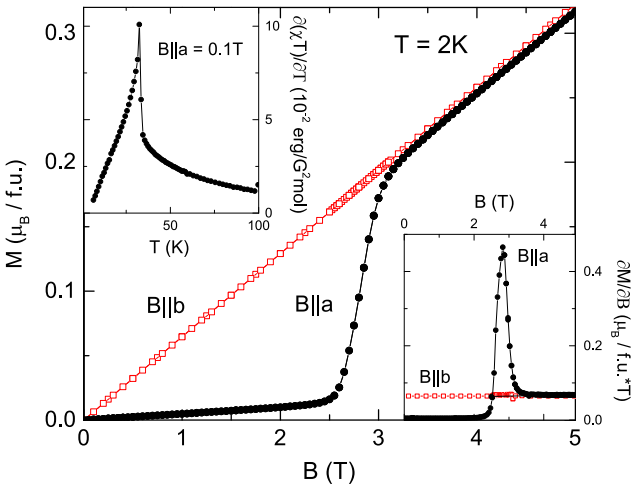

Fig. 6. Field dependence of the magnetization at $T=2$ K for $B\|a$ and $B\|b$. The upper inset shows the magnetic specific heat as calculated from the static susceptibility $\chi_{B\|b}(T)$, the lower inset presents the derivative $\partial M/\partial B$ of the data shown in the main plot.

Measurements of the static magnetic susceptibility $\chi=M/B$ vs. temperature are displayed in Fig. 5. For these measurements, a cuboid with size of $2.4\times2.5\times2.7$ mm^3 along the crystallographic *a*, *b*, and *c* directions was oriented and cut from the above mentioned cylindrical as-grown sample (compare Fig. 1). Note, that the inset of Fig. 5 also shows the magnetic susceptibility of a powdered piece of the single crystal for comparison. The data imply a paramagnetic Curie–Weiss-like behavior at high temperatures and long range antiferromagnetic order below $T_N=32.5$ K. At higher temperatures, the data can be described by applying the Curie–Weiss-law $\chi(T)=\chi_0+C/(T+\Theta)$, with the Curie constant *C*, a temperature-independent term $\chi_0=-3\times10^{-4}$ emu/(G^2 mol) and the Curie–Weiss temperature $\Theta\approx-70$ K. Fitting the data yields an effective magnetic moment of $p=5.99\mu_B$. Analyzing the magnetic specific heat, which is proportional to $\partial(\chi T)/\partial T$ (see upper inset of Fig. 6), shows that the onset of long-range magnetic order is associated with a pronounced and very clear lambda-like anomaly. In addition, there is a pronounced anisotropy of the magnetic susceptibility in the magnetically ordered phase that again signals the high quality of the crystal. This is also visible in the magnetic field dependence of the magnetization shown in Fig. 6. Upon application of B parallel to the easy magnetic *a*-axis, the data exhibit a clear and sharp spin–flop transition at $B_{SF}=2.8$ T. At this field, a spin-reorientation occurs so that the magnetic moments are mainly aligned perpendicular to the external field. Please note that this value is clearly reduced as compared to undoped $LiMnPO_4$ where $B_{SF}=4$ T [30]. For $B\|a > B_{SF}$, the magnetization curve is linear and extrapolates to zero, as expected for a spin–flop transition. It is noteworthy that the $M(B\|b)$ curve is a straight line in the accessible field range, which again is expected for an Neel-type antiferromagnetic order. However, any non-ordered impurity would cause a Brillouin-like field dependence, i.e. a right curvature at low-fields and fast saturation. The $M(B\|a)$ data at hand do not exhibit a clear non-linear contribution. Analyzing the data allows the quantitative estimation of the upper impurity limit to be as low as about $\approx2\times10^{-4}\mu_B$/f.u.

4. Conclusions

A $LiMn_{0.95}Ni_{0.05}PO_4$ single crystal has been grown by the floating zone technique. The grown crystal was carefully characterized by polarized microscopic images, X-ray Laue back scattering technique, X-ray powder diffraction, and the EDX method. An oriented cuboid with size of $2.4\times2.5\times2.7$ mm^3 along the *a*, *b*, and *c* crystalline directions was used for studies of the anisotropic magnetization.

Acknowledgments

The authors thank I. Glass, R. Müller, C. Malbrich, and K. Leger for experimental assistance. Support by the Bundesministerium für Bildung und Forschung (BMBF) within project 03SF0397 and by Deutsche Forschungsgemeinschaft DFG via KL1824/5, WU595/3-1, and GR3330/2 is gratefully acknowledged. KW acknowledges support by the European Commission through FP7 Marie Curie Grant PIIF-GA-2012-331476 LiCrystG.

References

[1] B.B. van Aken, J.P. Rivera, H. Schmid, M. Fiebig, Nature 449 (2007) 702.
[2] R. Toft-Petersen, et al., Physical Review B 85 (2012) 224415.
[3] J.-M. Tarascon, M. Armand, Nature 414 (2001) 359;
S.-Y. Chung, J.T. Bloking, Y.-M. Chiang, Nature Materials 1 (2002) 123;
S.P. Herle, B. Ellis, N. Coombs, L.F. Nazar, Nature Materials 3 (2004) 147.
[4] A. Vadivel Murugan, T. Muraliganth, P.J. Ferreira, A. Manthiram, Inorganic Chemistry 48 (2009) 946.
[5] C. Jähne, C. Neef, C. Koo, H.-P. Meyer, R. Klingeler, Journal of Materials Chemistry A 1 (2013) 2856.
[6] D. Wang, et al., Journal of Power Sources 189 (2009) 624.
[7] V. Aravindan, J. Gnanaraj, Y.-S. Lee, S. Madhavi, Journal of Materials Chemistry A 1 (2013) 3518.
[8] C. Neef, C. Jähne, H.-P. Meyer, R. Klingeler, Langmuir 29 (2013) 8054.
[9] M. Minakshi, S. Kandhasamy, Current Opinion in Solid State and Materials Science 16 (2012) 163.
[10] V.I. Formin, V.P. Gnezdilov, V.S. Kurnosov, A.V. Peschanskii, A.V. Yeremenko, H. Schmid, J.-P. Rivera, S. Gentil, Low Temperature Physics 28 (2002) 203.
[11] P.R. Elliston, J.G. Creer, G.J. Troup, Journal of Physics and Chemistry of Solids 30 (1969) 1335.
[12] J. Li, et al., Physical Review B 73 (2006) 024410.
[13] J. Li, T.B.S. Jensen, N.H. Andersen, J.L. Zarestky, R.W. McCallum, J.-H. Chung, J.W. Lynn, D. Vaknin, Physical Review B 79 (2009) 174435.
[14] D.P. Chen, A. Maljuk, C.T. Lin, Journal of Crystal Growth 284 (2005) 86;
R. Amin, J. Maier, P. Balaya, D.P. Chen, C.T. Lin, Solid State Ionics 179 (2008) 1683;
R. Amin, P. Balaya, J. Maier, Electrochemical and Solid-State Letters 10 (2007) A13;
R. Amin, J. Maier, Solid State Ionics 178 (2008) 1831.
[15] R. Amin, C.T. Lin, J. Peng, K. Weichert, T. Acartürk, U. Starke, J. Maier, Advanced Functional Materials 19 (2009) 1697.
[16] R. Amin, C.T. Lin, J. Maier, Physical Chemistry Chemical Physics 20 (2008) 3519. (ibid. 3524 (2008).
[17] R. Saint-Martin, S. Franger, Journal of Crystal Growth 310 (2008) 861.
[18] N. Wizent, G. Behr, F. Lipps, I. Hellmann, R. Klingeler, V. Kataev, W. Löser, N. Sato, B. Büchner, Journal of Crystal Growth 311 (2009) 1273.
[19] N. Wizent, G. Behr, W. Löser, B. Büchner, R. Klingeler, Journal of Crystal Growth 318 (2011) 995.
[20] T. Roisnel, J. Rodriguez-Carvajal, Materials Science Forum 378–381 (2001) 118.
[21] O. García-Moreno, M. Alvarez-Vega, F. García-Alvarado, J. García-Jaca, J.M. Gallardo-Amores, M.L. Sanjuán, U. Amador, Chemistry of Materials 13 (2001) 1570.
[22] R. Allmann, R. Hinek, Acta Crystallographica A 63 (2007) 412.

[23] CrysAlisPro, Agilent Technologies UK Ltd., Oxford, 2011.
[24] R.H. Blessing, Acta Crystallographica A51 (1995) 33;
R.H. Blessing, SCALE3 ABSPACK, CrysAlisPro, Agilent Technologies UK Ltd., Oxford, 2011.
[25] (a) G. Oszlányi, A. Sütö, Acta Crystallographica A60 (2004) 134;
(b) G. Oszlányi, A. Sütö, Acta Crystallographica A61 (2005) 147.
[26] G.M. Sheldrick, SHELXT, University of Göttingen, 2013.
[27] (a) G.M. Sheldrick, SHELXL-2013, University of Göttingen, 2013;
(b) G.M. Sheldrick, Acta Crystallographica A64 (2008) 112.
[28] Fachinformationszentrum Karlsruhe, 76344 Eggenstein-Leopoldshafen, Germany (crysdata@fiz-karlsruhe.de, ⟨http://www.fiz-karlsruhe.de/request_for_deposited_data.html⟩).
[29] R.D. Shannon, Acta Crystallographica A 32 (1976) 751.
[30] J.H. Ranicar, P.R. Elliston, Physics Letters A 25 (1967) 720.